Self-consistent simulations of nonlinear magnetohydrodynamics and profile evolution in stellarator configurations

M.G. Schlutt,[1] C.C. Hegna,[1] C.R. Sovinec,[1] E.D. Held,[2] and S.E. Kruger[3]

[1)] *University of Wisconsin-Madison, 1500 Engineering Dr., Madison, WI*[a)]

[2)] *Utah State University, Logan, UT*

[3)] *Tech-X Corporation, 5621 Arapahoe Ave., Boulder, CO*

(Dated: 30 November 2012)

Self-consistent MHD equilibrium and nonlinear stability of 3D magnetic configurations are investigated using an extended MHD framework. In these calculations, initial conditions are given by analytical 3-D vacuum solutions. Finite beta discharges in a straight stellarator are simulated. Vacuum magnetic fields are applied to produce stellarator-like rotational transform profiles with iota(0)$\leq$0.5 and iota(0)$\geq$0.5. The vacuum magnetic fields are either helically symmetric or spoiled by the presence of magnetic harmonics of incommensurate helicity. As heat is added to the system, pressure-driven instabilities are excited when a critical β is exceeded. These instabilities may grow to large amplitude and effectively terminate the discharge, or they may saturate nonlinearly as the equilibrium evolves. In all of these studies, anisotropic heat conduction is allowed with $\kappa_\parallel/\kappa_\perp = 10^4 - 10^7$. Due to the finite parallel heat conduction, in some cases an equilibrium state persists that has a stochastic edge region which supports a pressure gradient.

PACS numbers: 52.65.Kj, 52.55.Hc, 52.30.Cv

[a)]Electronic mail: mgschlutt@wisc.edu

I. INTRODUCTION

Over the past decade large stellarator experiments have achieved values of beta which are higher than the maximum beta predicted by linear ideal MHD stability calculations.[1,2] As beta increases, the predicted instabilities appear as the stability boundaries are traversed, but the self-consistent modification of the equilibrium profiles allows these instabilities to saturate nonlinearly.[3,4] Here, the maximum achievable beta is not simply related to ideal MHD instability onset, but rather intimately connected to the modification of the equilibrium. This behavior is in sharp contrast to tokamak operation where beta is limited by stability considerations, with disruptions occurring when long wavelength ideal MHD stability boundaries are crossed.[5] This modification of the equilibrium in response to emerging instabilities and the subsequent equilibrium-related beta-limiting effects are perhaps enabled by the intrinsic 3-D nature of equilibrium quantities in a stellarator.

MHD equilibrium of axisymmetric devices is well described by Grad-Shafranov theory. Stability of these equilibria is accurately predicted by linear analysis. However, Grad-Shafranov theory is not suitable for describing 3-D equilibria since well-formed flux surfaces are not guaranteed for 3-D magnetic field structures.[6] Many attempts have been made to develop analysis tools to determine 3-D equilibrium field structure and subsequent stability characteristics.[7–13] Although some of these tools can allow for 3-D magnetic features like islands or stochastic regions[14–17], not all of the profiles are calculated self-consistently, transport effects are not always included, and there is no general consensus on how to properly constrain the profiles for general magnetic topology.[18] Furthermore, non-magnetostatic physical effects, like that of plasma flows, add further complexity to this modeling problem.[19–21] The problem of emerging instabilities demands a self-consistent analysis since the concepts

of equilibrium and stability become intertwined, with the equilibrium field structure changing in response to emerging instabilities. Time-dependent extended MHD modeling provides a framework for combining dynamics with transport effects and efforts to describe stellarators with extended MHD modeling are underway.[22] In this work, we demonstrate how the NIMROD code can be utilized to study high-beta stellarators.

Ichiguchi and Carreras utilize another approach to simulate discharges in the Large Helical Device (LHD) where beta values increased through predicted stability boundaries.[3] Their algorithm determines the nonlinear dynamics through an iterative method, using reduced MHD equations to provide transport information and updates to the magnetic field structure from the VMEC code.[8] This algorithm is successful in reproducing the behavior of saturating resonant interchange instabilities in LHD, for low values of beta. For these resonant modes, Ichiguchi proposes a mechanism by which the pressure flattens locally about the resonant surface, enhancing transport and limiting the drive for instability growth. However this mechanism does not explain how non-resonant modes might be stabilized.

Here we address the temporal evolution of finite-beta discharges in straight stellarator configurations using self-consistent 3-D nonlinear computation with the NIMROD code.[23] The straight stellarator configuration is chosen for several reasons. First, analytical solutions for the vacuum magnetic field exist for the straight stellarator. This provides for flexibility in specifying the vacuum magnetic field, and consequently the rotational transform profile is easily prescribed. Also, the straight stellarator is chosen because of its sensitivity to interchange modes. Since toroidal curvature is absent, there is bad curvature associated with the poloidal magnetic field curvature. Also contributing to the sensitivity to interchange modes is the lack of a Shafranov shift with increasing beta in a straight configuration. In toroidal configurations like LHD, a Shafranov shift occurs with increasing beta, thereby

creating a magnetic well near the core. In this present straight stellarator configuration, no magnetic well develops with increasing beta. Because of these reasons, maximum values of beta reached in these simulations are significantly lower than in present-day stellarator experiments. However, the evolution of the equilibrium in response to emerging instabilities is still a prominent feature of these discharges.

To investigate how the 3-D nature of the equilibrium quantities affects the evolution of the equilibrium in response to emerging instabilities, two classes of vacuum magnetic fields for this straight stellarator are studied. The first class of vacuum configurations is the helically symmetric magnetic field. Helically symmetric equilibria are 2-D, and as a result they can be rigorously described by Grad-Shafranov theory. These helically symmetric cases are heated and the discharge evolution is observed. In the second class of configurations, helically symmetric cases are spoiled with the addition of small harmonics to the vacuum magnetic field which are incommensurate with the previously helically symmetric field. The addition of these small symmetry-spoiling harmonics to this helically symmetric configuration allows the configuration to retain much of the favorable characteristics of helical symmetry, but still have the effect of interrupting the closed flux surfaces, especially near the edge. These spoiled symmetry cases are subsequently heated, and the discharge evolution is compared to their helically symmetric counterparts. Also investigated is the effect of changing the structure of the helically symmetric vacuum magnetic field. Here, finite beta results are reported for three different vacuum rotational transform profiles.

It is well known that the physics of 3-D magnetic islands is affected by the degree of anisotropic transport.[24–26] Additionally, stochastic regions in stellarators which support a pressure gradient have been observed, indicating finite transport along field lines.[4] Here, the effect of changing the degree of anisotropic transport is investigated for these heated straight

stellarator cases. Using the NIMROD code's diffusive model for anisotropic heat transport, and a small but finite viscosity, larger and smaller ratios of $\kappa_\parallel/\kappa_\perp$ are applied and discharge evolution is observed. The relationship between changing this anisotropic transport ratio and changing the magnitude of the symmetry-spoiling harmonics is explored.

The procedure for how the vacuum magnetic field in a straight stellarator is calculated using the NIMROD code is presented in Section II. In Section III, discharge evolution results are presented for a few interesting finite β cases. In Section IV computational results are presented which show how the addition of symmetry-spoiling harmonics affects the discharge evolution, and results are shown for cases where the ratio of $\kappa_\parallel/\kappa_\perp$ is changed. Finally, in Section V, the implications of these results are discussed.

II. LOADING OF A NON-AXISYMMETRIC FIELD

In vacuum there are no currents, $\nabla \times \boldsymbol{B} = 0$, so the magnetic field can be represented as the gradient of a scalar potential, $\boldsymbol{B} = \nabla\phi$. Since the magnetic field is solenoidal, $\nabla \cdot \boldsymbol{B} = 0$, the resulting Laplace equation, $\nabla^2\phi = 0$, can be solved in a periodic cylinder:[27]

$$\phi = B_0 \left[R\zeta + \sum_m \epsilon_m \frac{Rm}{n} I_m \left(\frac{nr}{R}\right) \sin(m\theta - n\zeta) \right] \tag{1}$$

where B_0 is the uniform guide field in the axial direction, ζ is the axial coordinate distance, m and n are the poloidal and axial ("toroidal") mode numbers respectively, ϵ_m is the strength of mth harmonic relative to B_0, r is the radial distance from the geometric center, θ describes the distance in the azimuthal direction, I_m is the modified Bessel function of order m, and R provides a measure of the length of the periodic cylinder where $L = 2\pi R$. Eq.(1) can represent vacuum magnetic fields for any combination of harmonics, m, n. Cases where ϕ in Eq.(1) consists of a single m, n harmonic (and multiples of that harmonic) are called

"helically symmetric".

At the beginning of these simulations the magnetic field at the computational boundary of the periodic cylinder is calculated from Eq.(1). The normal component of the magnetic field at the wall from this vacuum solution is not allowed to evolve in time, i.e.

$$\frac{d}{dt}\boldsymbol{B}\cdot\hat{\boldsymbol{n}}|_{\text{bdry}} = 0. \tag{2}$$

With this initialization and no applied heating, the vacuum magnetic field structure persists in time as expected. An example of typical equilibrium created by this algorithm is shown in Figure 1. Here, several "toroidal" slices are shown for a helically symmetric $m = 2$, $n = 2$, $\epsilon_{22} = 0.8$ configuration. The rotational transform for this configuration is shown in Figure 2.

As a check to ensure that this field is computed correctly, we have verified that the magnitude of $\nabla\cdot\boldsymbol{B}$ as computed by the NIMROD code has zero value to machine precision. Additionally, vacuum magnetic fields generated in NIMROD with this technique have been perturbed. The perturbations die away as time passes (since there is finite dissipation), leaving the original vacuum magnetic field.

To study finite β effects, it is necessary to move beyond the simple vacuum magnetic field structure specified by Equation 1. This is accomplished in the NIMROD code by adding a volumetric ad-hoc heating source. This heat source is defined with magnitude constant on each flux surface of the dominant helically symmetric vacuum magnetic field. This heating rate evolves in time based on a hyperbolic tangent function. That is, the heating source ramps up from a starting value to a user-defined maximum in time, based on user-defined settings which control the slope of the ramp-up and the specific time when the ramp-up occurs.

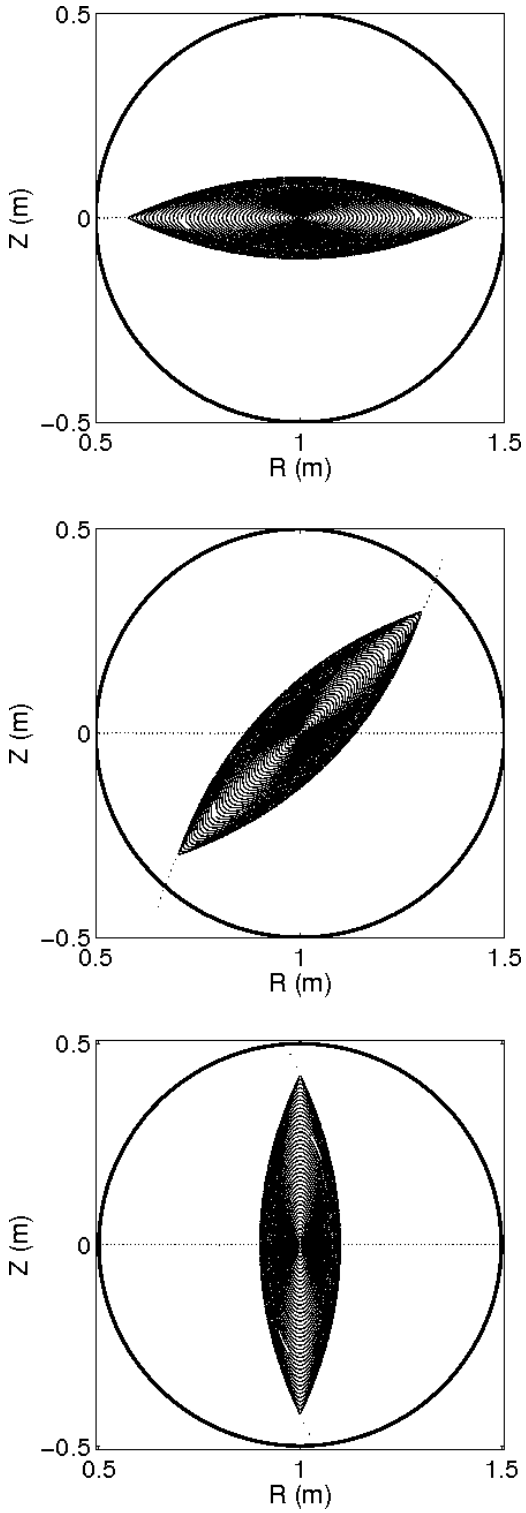

FIG. 1. Poincaré plots for vacuum m=2, n=2, $\epsilon_{22} = 0.8$ at $\zeta = 0$ (top), $\zeta = \pi/4$ (middle) and $\zeta = \pi/2$ (bottom).

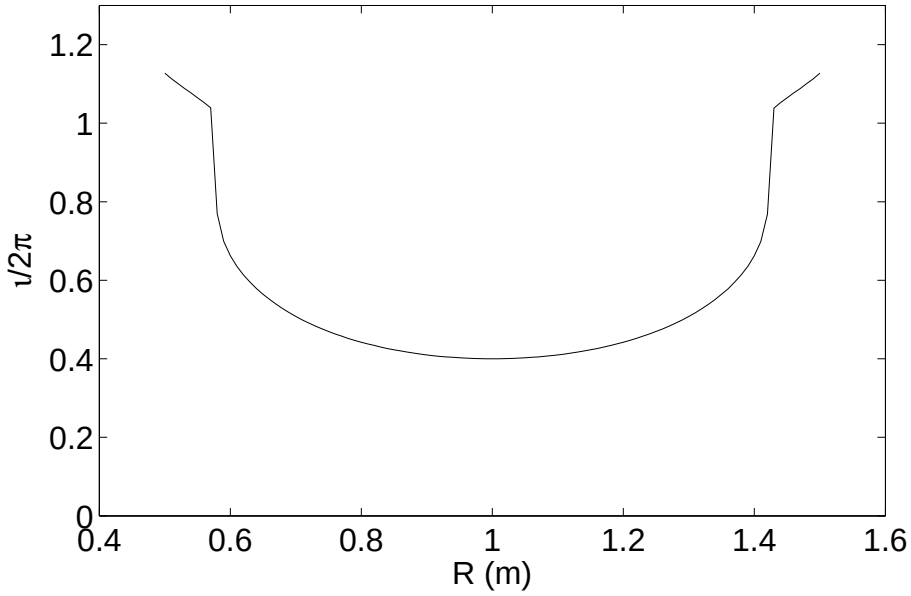

FIG. 2. Vacuum rotational transform for m=2, n=2, $\epsilon_{22} = 0.8$ at $\zeta = 0$. In this plot, closed flux surfaces extend from R= 0.58m to R= 1.42m.

III. FINITE BETA CALCULATIONS OF A STRAIGHT STELLARATOR

Various heating rates are applied to m=2, n=2 helically symmetric cases and spoiled symmetry cases, and the results are compared. Several parameters are varied for these investigations. While a variety of vacuum configurations have been simulated, in the following we will primarily describe simulations with $\epsilon_{22} = 0.85$, which produces $\iota(0) \lesssim 0.5$, and $\epsilon_{22} = 0.87$, which produces $\iota(0) \gtrsim 0.5$. These two configurations are chosen due to the role of n/m=1/2 modes relative to whether an $\iota = 1/2$ surface exists within the plasma or not. The heating profile is specified as maximum at $r = 0$ (core), decreasing linearly to 0 at the last closed flux surface. For these investigations, the maximum volumetric heating rates range from 2 MW/m^3 at $r = 0$ to 16 MW/m^3 at $r = 0$. The ratio of parallel conductivity to perpendicular conductivity ($\kappa_\parallel/\kappa_\perp$) is varied from 10^4 to 10^7, though most of these calculations have $\kappa_\parallel/\kappa_\perp = 10^6$. Finally, these calculations were performed with a Lundquist number of

438,000 (using vessel minor radius as scale length) and a magnetic Prandtl number of 1.

For these simulations, 22 toroidal Fourier components ($0 \leq n \leq 21$) are used. In the poloidal plane, the simulation mesh consists of 24 radial and 32 poloidal bi-quartic finite elements, which implies node spacing on the order of 5 mm.

From many conditions simulated so far, the two cases are presented here to illustrate the behavior of two broad classes of configurations, those with resonant mode growth and those with non-resonant mode growth. Also, these particular cases are chosen to show two qualitatively different types of equilibrium evolution. In one instance the instability grows and eventually destroys confinement, while in the other case presented, the instability saturates nonlinearly after a period of linear growth.

A. m=2, n=2, $\epsilon_{22} = 0.85$

This configuration has core vacuum rotational transform of $\iota(0) = 0.473$ as shown in Figure 3. Other parameters for this configuration are an effective minor radius of $a_{\text{eff}} = 0.159$m, confinement time of $\tau_E = 4.37$ms, and Alfv́en time of $\tau_A = 1.61\mu$s. Here, results are presented for the helically symmetric case.

For peak heating strength of 4 MW/m^3, the heating is observed to modify the rotational transform via diamagnetism, especially near the core, as shown in Figure 4. Early in this simulation, as the rotational transform assumes values of low order rational numbers, islands form. However, values of beta and pressure gradient are quite low at this early time, so these islands subsequently heal or saturate. Later in time when beta is higher, as the rotational transform profile becomes flatter near the core and the stabilizing effect of the shear is lost, an m=2, n=1 island structure appears as shown in Figure 5. As time progresses, these islands grow and eventually destroy all flux surfaces, after achieving a peak beta of 1.54%

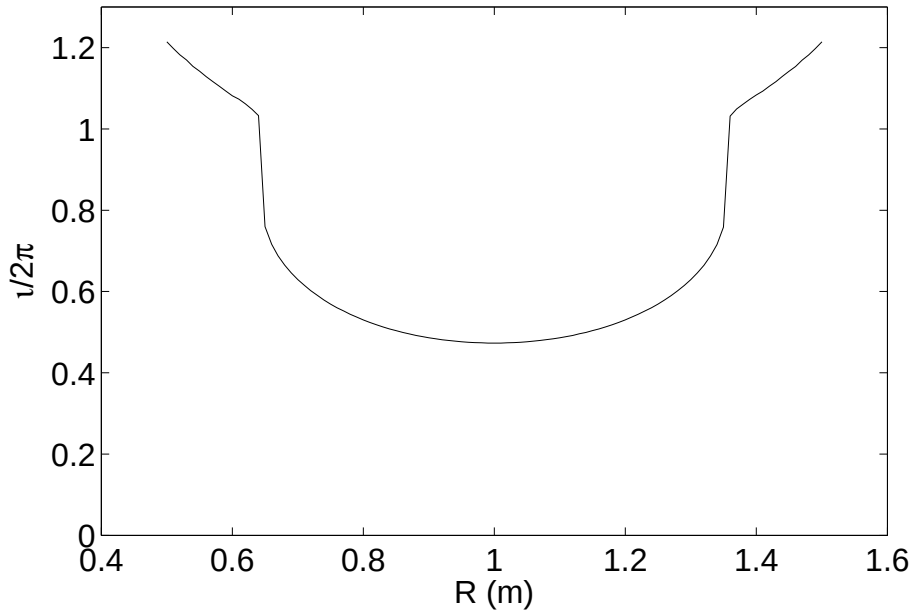

FIG. 3. Vacuum rotational transform for the m=2, n=2, $\epsilon_{22} = 0.85$ helically symmetric case. Closed flux surfaces exist for 0.65<R<1.35.

at $t = 1.97$ms. The instability appears at $\beta_{\text{onset}} = 1.44\%$ and the estimated linear growth rate is $\gamma\tau_A = 0.017$.

This profiles of rotational transform in time provide insight into understanding the mode appearance and growth. The m=2, n=1 surface is located within the plasma, at approximately R=0.86 and R=1.14 (on the $\zeta = 0$ plane) as can be seen in Figures 3 and 4. However, since beta is so low early in this discharge, there is not enough drive to trigger mode growth with respect to this rational surface. As the plasma is heated, the rotational transform is modified and becomes flatter across the core region. At the same time, beta has increased to above some MHD critical limit. This triggers the formation of a resonant core mode, in this case at the m=2, n=1 surface.

An examination of the poloidal and toroidal decomposition of the parallel current at

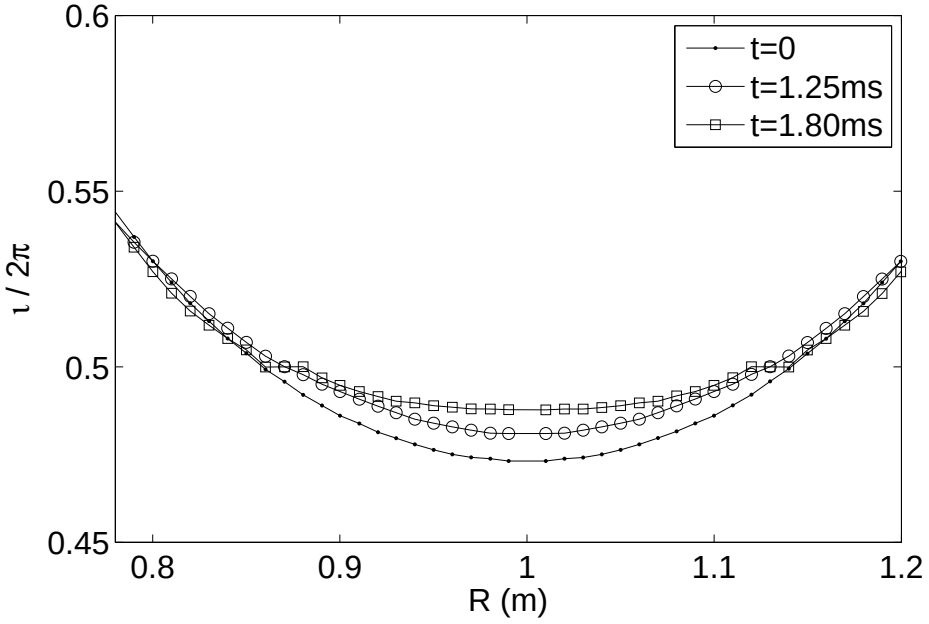

FIG. 4. Rotational transform for the m=2, n=2, $\epsilon_{22} = 0.85$ helically symmetric, 4 MW/m^3 heating strength case at various times. Shear is lost in the core as time progresses. Island formation at R=0.86 m and R=1.14 m results in flattening of the transform profile.

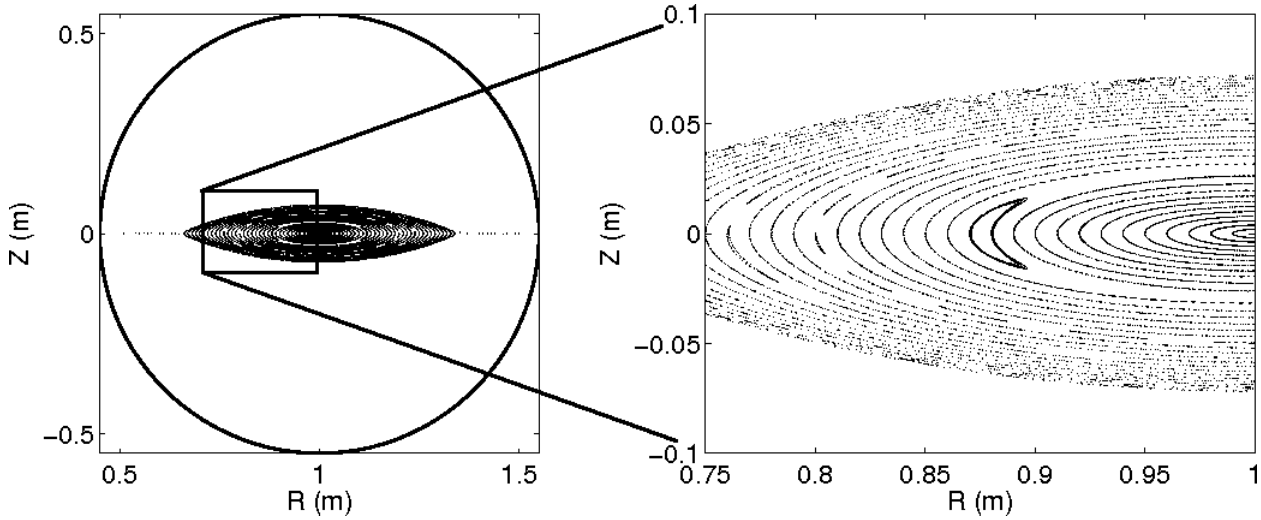

FIG. 5. Poincaré plot for the helically symmetric, 4 MW/m^3 heating strength m=2, n=2, $\epsilon_{22} = 0.85$ case at $t = 1.75$ms, $\zeta = 0$. Note the prominent m=2, n=1 structure.

$t = 1.94$ms is shown in Figure 6. Here, the parallel current, $\lambda = \boldsymbol{J} \cdot \boldsymbol{B}/B^2$ is decomposed as

$$\lambda(r,\theta,\phi) = \sum_{n=0}^{+\infty}\sum_{m=0}^{+\infty}[A_{mn}(r)\cos(m\theta - n\phi) + B_{mn}(r)\sin(m\theta - n\phi) + C_{mn}(r)\cos(m\theta + n\phi) + D_{mn}(r)\sin(m\theta + n\phi)] \quad (3)$$

where A_{mn} and B_{mn} are the amplitudes of the positive helicity components and C_{mn} and D_{mn} are the amplitudes of the negative helicity components. The mode localization shown in Figure 6 is similar to that observed in previous cylindrical eigenmode calculations of straight stellarator configurations[28]. Modes which are resonant display localized structure, whereas modes which are non-resonant display broad structure.

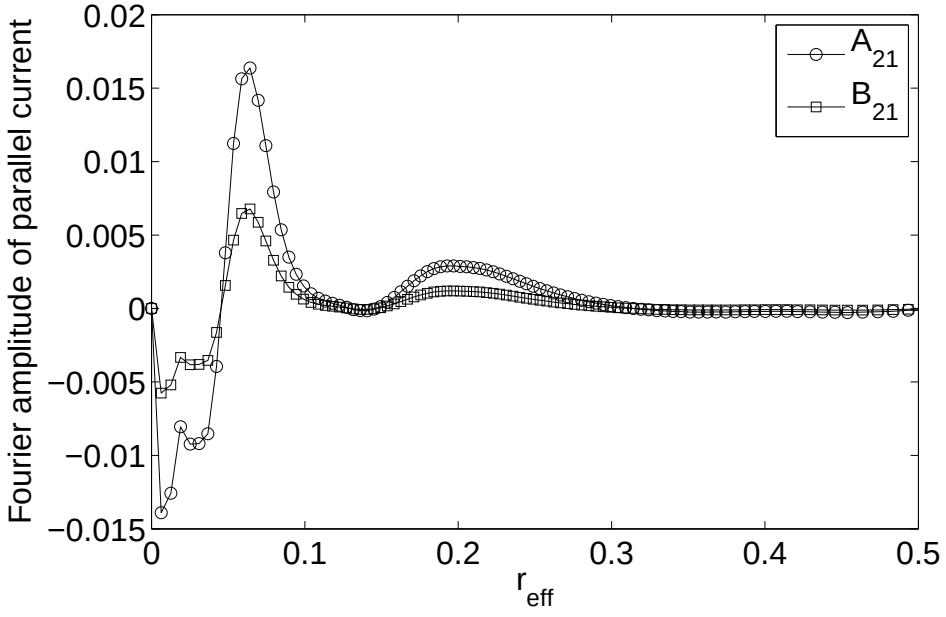

FIG. 6. Amplitude of selected Fourier harmonics of parallel current for the helically symmetric m=2, n=2, $\epsilon_{22} = 0.85$, 4 MW/m^3 heating strength case at $t = 1.94$ms. Note the localization, indicating resonant mode structure. Here, r_{eff} is an effective radius, which results from Fourier sampling in the aziumuthal direction and the fact that the lenticular magnetic flux surfaces helically twist as the azimuthal direction is traversed.

B. m=2, n=2, $\epsilon_{22} = 0.87$

This configuration has core vacuum rotational transform of $\iota(0) = 0.507$ as shown in Figure 7. Other parameters for this configuration are a minor radius of $a_{\text{eff}} = 0.140$m, confinement time of $\tau_E = 3.40$ms, and Alvfén time of $\tau_A = 1.61\mu$s. For this configuration, various heating rates are used, ranging from 2 MW/m^3 up to 16 MW/m^3 on the magnetic axis. Only the higher heating rates produce abrupt disruptive responses. The lower heating rates develop a mode which does not succeed in destroying the confinement.

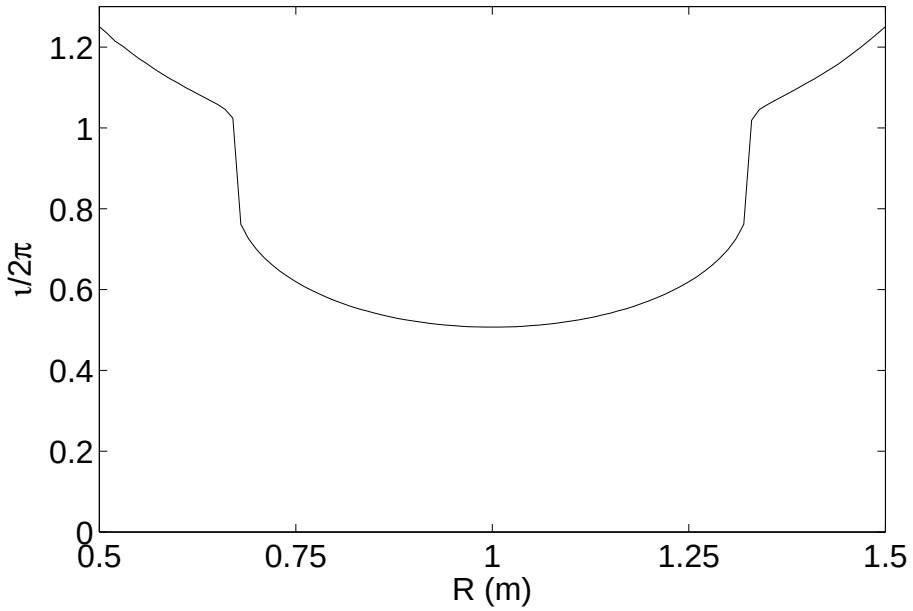

FIG. 7. Vacuum rotational transform for the m=2, n=2, $\epsilon_{22} = 0.87$ helically symmetric case. Closed flux surfaces exist for 0.68<R<1.32.

For the helically symmetric case a heating strength of 4 MW/m^3 is applied. The discharge evolution is significantly different from the higher heating rate cases which disrupt. At $t = 2.42$ms, mode growth begins, as $\beta_{\text{onset}} = 1.63\%$ reached. This mode growth is dominated by m=2, n=1 and m=0, n=1 non-resonant components, but grows relatively slowly, with

$\gamma\tau_A = 0.007$. Additionally, this mode nonlinearly saturates, rather than directly causing a disruption. This is illustrated in Figure 8, which shows time evolution of the n=1 component of the kinetic energy. The maximum value of beta achieved for this case is 1.65%.

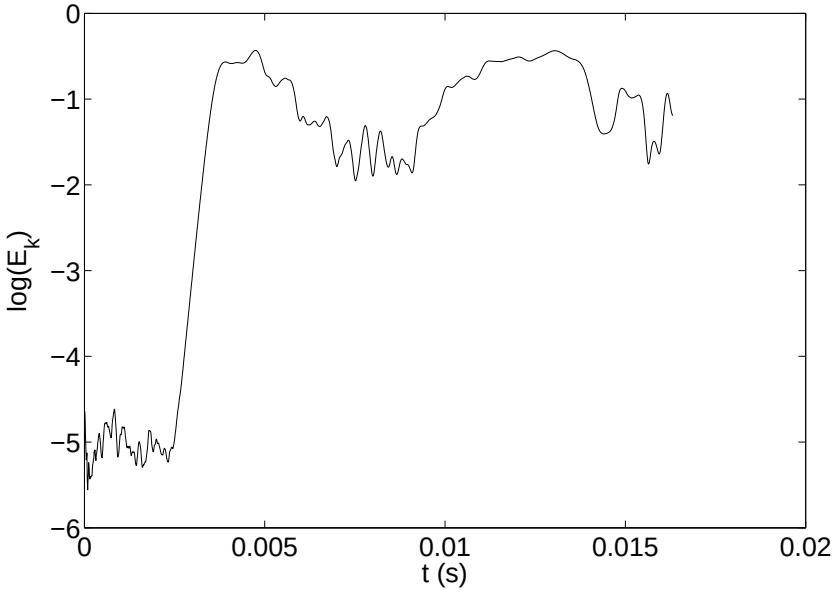

FIG. 8. Kinetic energy for the n=1 component for the helically symmetric m=2, n=2, $\epsilon_{22} = 0.87$, 4 MW/m^3 heating strength case. The growing mode nonlinearly saturates.

The evolution of the magnetic topology for this case exhibits a sequence of relaxation oscillations. Figure 9 shows Poincaré plots which illustrate how the m=2, n=1 structure appears and how the equilibrium responds to this mode. This behavior continues, as the magnetic topology oscillates between a coherent m=2, n=1 structure (which is sometimes toroidally phase-shifted by $\zeta = \pi$) and topology with more well-formed flux surfaces in the core region. During this time, as shown in Figure 10, the rotational transform profile first rises as the m=2, n=1 mode grows. After significant mode growth, the rotational transform then falls in the core, nearing $\iota = 0.5$, before rising slightly again.

Late in time, after about 4 confinement times, the magnetic topology is still oscillating

between a coherent m=2, n=1 structure (which is sometimes toroidally phase-shifted by $\zeta = \pi$) and topology with more well-formed flux surfaces in the core region. A representative Poincaré plot is shown in Figure 11. Note that there is a stochastic region near the edge. This region continues to support a pressure gradient as shown in Figure 12. Clearly, this ability to support a pressure gradient in a stochastic region is closely related to the degree of anisotropic heat conduction and the small but finite viscosity present in the simulation. This effect will be covered in more detail in Section IV B, where simulation results are presented which are run with varying ratios of parallel to perpendicular heat diffusivities.

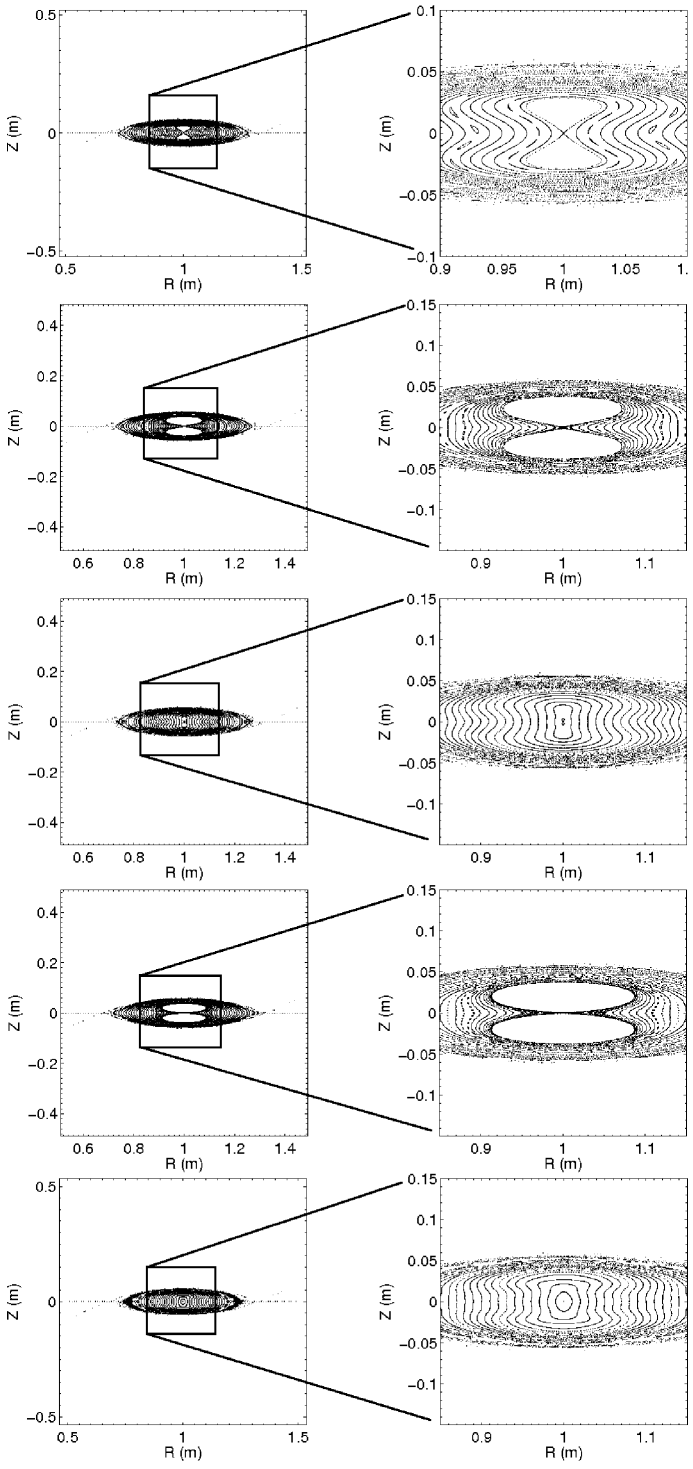

FIG. 9. Poincaré plots for the m=2, n=2, $\epsilon_{22} = 0.87$ helically symmetric case at $\zeta = 0$, with peak heating strength of 4 MW/m^3. These snapshots show 0.5 ms intervals ranging from $t = 3.50$ ms (top) to 5.50 ms (bottom). Here, an m=2, n=1 structure has forms, but well-formed flux surfaces are recovered, and the cycle repeats.

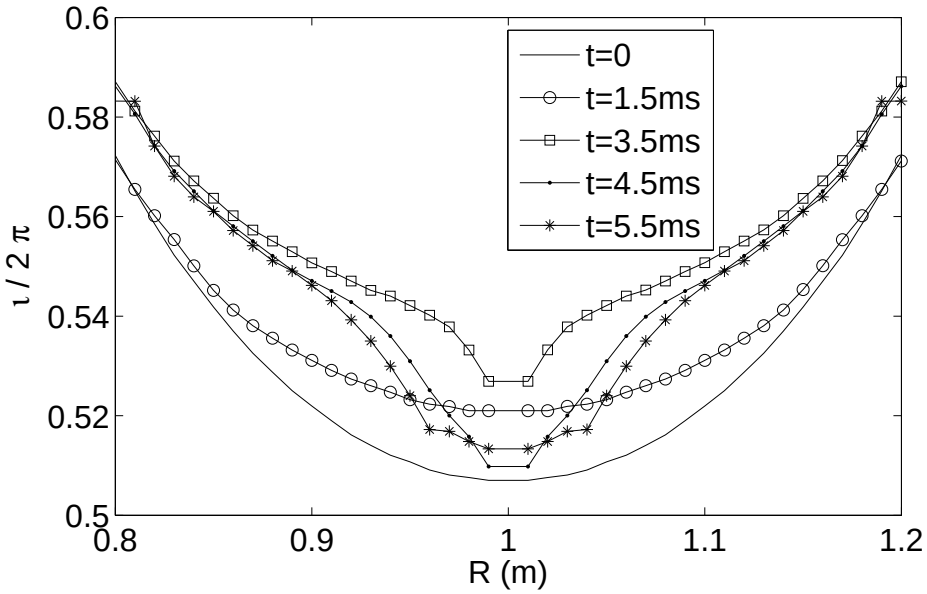

FIG. 10. Rotational transform for the m=2, n=2, $\epsilon_{22} = 0.87$, 4 MW/M^3 heating strength, helically symmetric case at various times. The central part of the rotational transform first becomes shearless, drops toward 0.5, then begins to rise again as flux surfaces are recovered in the core.

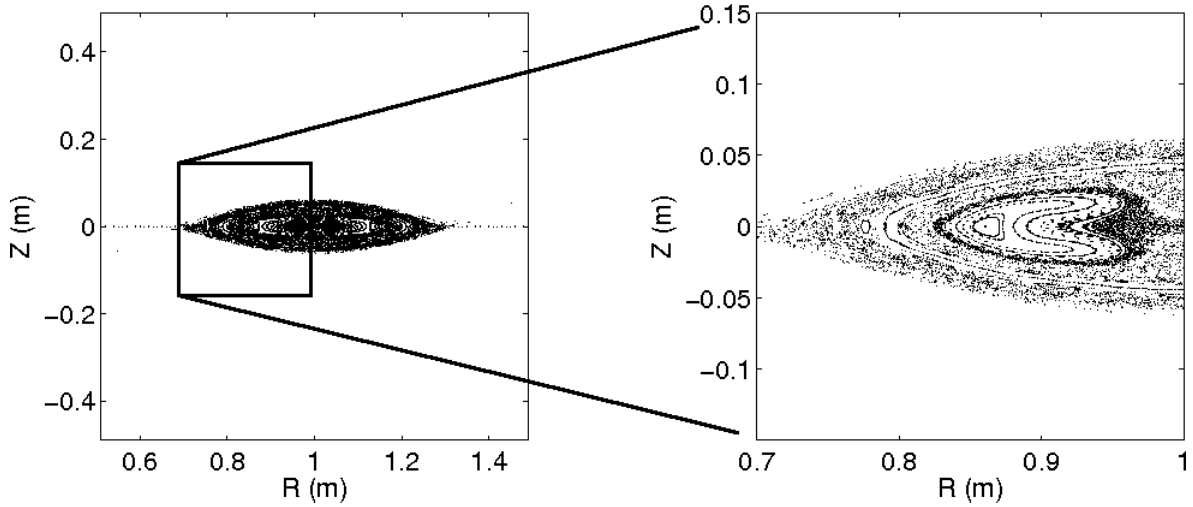

FIG. 11. Poincaré plot for the m=2, n=2, $\epsilon_{22} = 0.87$ helically symmetric case at $\zeta = 0$, $t = 15.79$ms, with heating strength of 4 MW/m^3. Note the stochastic region near the edge.

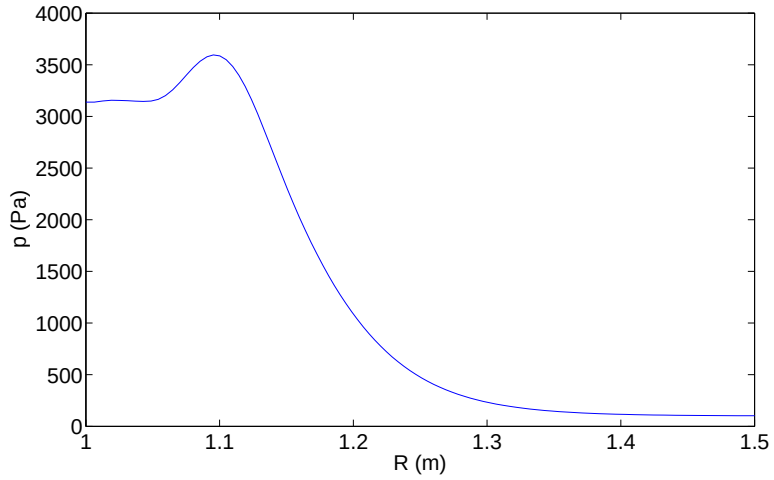

FIG. 12. Pressure profile for the helically symmetric m=2, n=2, $\epsilon_{22} = 0.87$, 4 MW/m^3 heating strength case at $t = 15.79$ms. Here, the magnetic axis is at R=1m. The region outside R=1.20m does not have well-formed flux surfaces. Note that there is a gradient supported in this region.

IV. THE EFFECT OF SYMMETRY-SPOILING HARMONICS

A. Summary of the m=2, n=2 configurations

Here, results are given for two configurations which are simulated: $\epsilon_{22} = 0.85$, and $\epsilon_{22} = 0.87$. In these simulations, the performance of helically symmetric cases is compared with that of cases with spoiled symmetry. The effect on beta evolution and associated linear growth rate of adding symmetry-spoiling harmonics to a helically symmetric configuration is reported.

For the cases presented here, the symmetry-spoiling harmonics are chosen so that low order resonances with the dominant m=2, n=2 magnetic field are avoided. And, these symmetry-spoiling harmonics are chosen with strengths which range from $b_{ss}/B = 0.0001$ to $b_{ss}/B = 0.01$. As will be shown, these symmetry-spoiling harmonics have very little effect on the global confinement properties of the equilibrium. The key difference appears to be the small increase in magnetic energy for specific n-harmonics associated with the symmetry-spoiling harmonics.

1. $m = 2$, $n = 2$, $\epsilon_{22} = 0.85$

The core rotational transform for this configuration is $\iota(0) = 0.473$. Some differences between the helically symmetric cases and the spoiled symmetry cases are observed, although an m=2, n=1 resonant mode appears and destroys confinement in all cases. For these cases, the addition of symmetry-spoiling harmonics results in earlier mode formation and earlier disruption as shown in Figure 13. Furthermore, the addition of symmetry-spoiling harmonics results in slower mode growth as shown in Figure 14. This slower mode growth is related to the earlier appearance of the instability. Since the instability appears at a lower beta, there

is less drive for growth, and the mode grows more slowly.

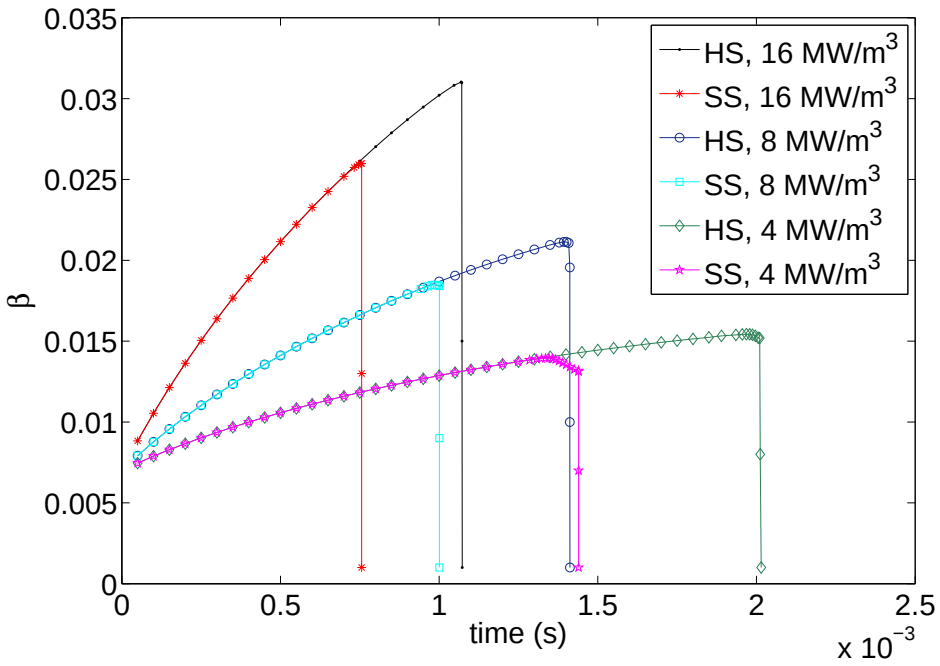

FIG. 13. (Color online) Beta evolution for the m=2, n=2, $\epsilon_{22} = 0.85$ cases. Here, the helically symmetric ("HS") and the spoiled symmetry ("SS") cases ($\epsilon_{5,1} = \epsilon_{6,1} = \epsilon_{6,5} = 0.01$) are coincident early in the discharge, with the spoiled symmetry cases disrupting sooner than the helically symmetric cases.

2. $m = 2,\ n = 2,\ \epsilon_{22} = 0.87$

The core rotational transform for this configuration is $\iota(0) = 0.507$. The highest heating cases, 16 MW/m^3 and 8 MW/m^3, display similar behavior. Both cases develop an m=2, n=1 non-resonant mode which grows and destroys all flux surfaces. The discharge evolution is qualitatively similar between the helically symmetric and spoiled symmetry cases, as shown in the pressure profile evolution of Figure 15. The key difference here is quantitative, as the helically symmetric case reaches higher pressures whereas the spoiled symmetry case reaches lower core pressures. The reason for this difference is that the spoiled symmetry

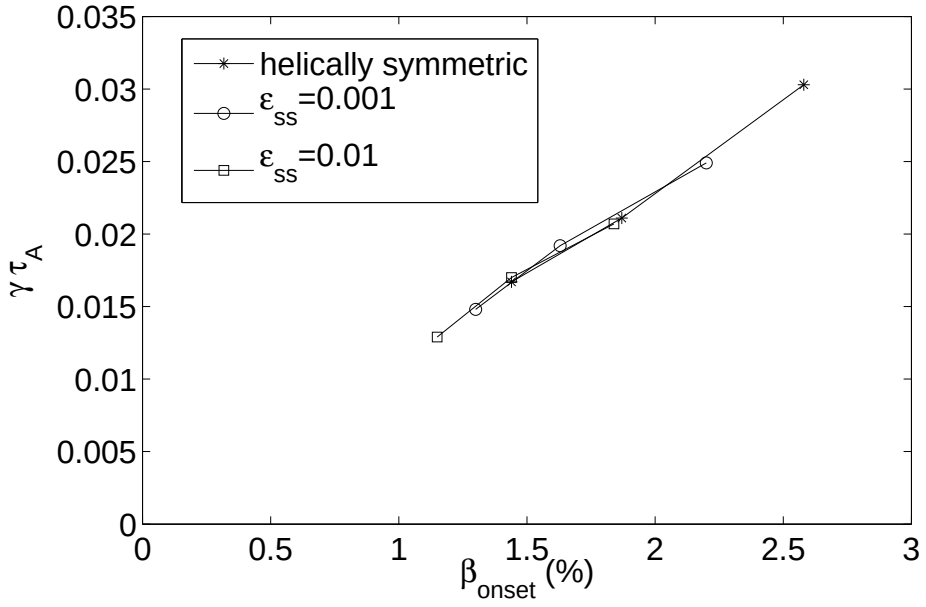

FIG. 14. Relationship between growth rate and β_{onset} for the m=2, n=2, $\epsilon_{22} = 0.85$ cases. The three data points for each series correspond to the three different heating rates. The largest heating rates result in the largest growth rates.

case develops a deleterious mode sooner which causes earlier loss of confinement as can be seen in Figure 16. The addition of symmetry-spoiling harmonics triggers earlier mode formation at lower beta, although the growth rates are similar as shown in Figure 17.

For the 4 MW/m^3 cases, which were highlighted in Section III B, no disruption is observed in either the helically symmetric case or the spoiled symmetry cases. In both cases, an m=2, n=1 non-resonant structure initially forms. After this initial mode appearance, the magnetic equilibrium oscillates between a state with the non-resonant structure (sometimes toroidally phase shifted by $\zeta = \pi$) and one with recovered, well-formed flux surfaces in the core region. This oscillation continues for the entire length of the simulations which were run ($\sim 4\tau_E$), showing no sign of disrupting or settling into a single quiescent configuration. The biggest difference between the spoiled symmetry case and the helically symmetric case is that the

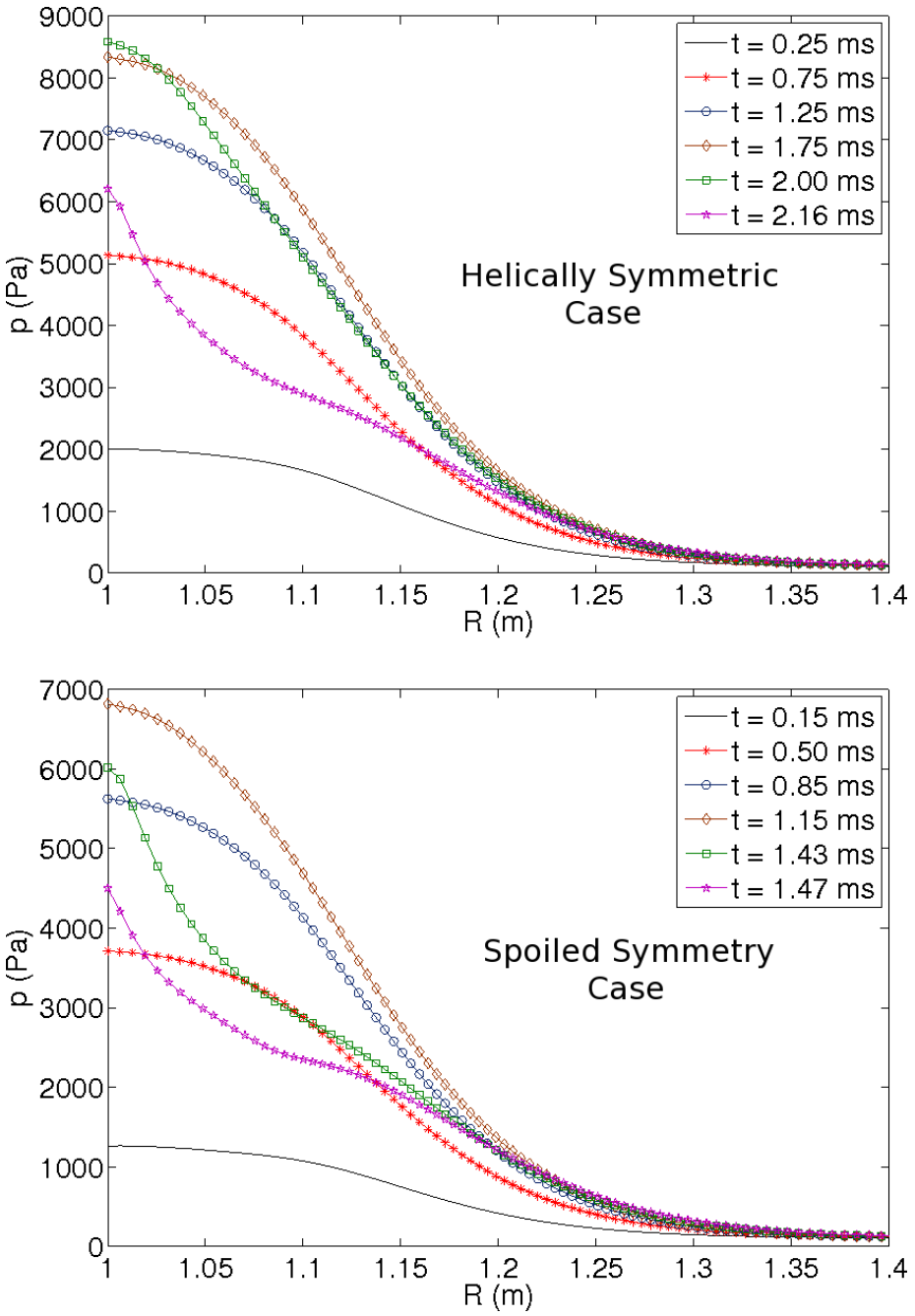

FIG. 15. (Color online) Pressure profiles of helically symmetric (top) and spoiled symmetry (bottom) 8 MW/m^3 m=2, n=2, $\epsilon_{22} = 0.87$ cases at selected times, $\zeta = 0$. When the m=2, n=1 non-resonant mode forms, heat is quickly pumped out of the system. Here, the magnetic axis is at R=1m.

case with spoiled symmetry has lower β_{onset} and earlier development of the m=2, n=1 mode. However, both the helically symmetric and spoiled symmetry cases achieve the same final,

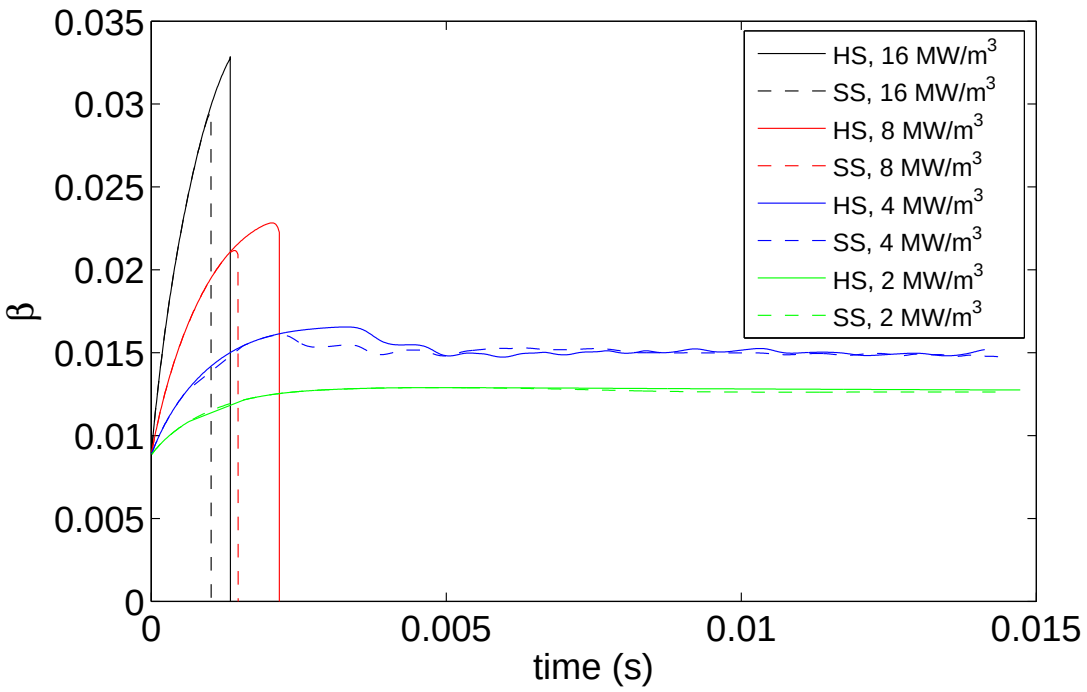

FIG. 16. (Color online) Beta evolution for the m=2, n=2, $\epsilon_{22} = 0.87$ dominant harmonic cases. Here, the helically symmetric ("HS") and the spoiled symmetry ("SS") cases ($\epsilon_{5,1} = \epsilon_{6,1} = \epsilon_{6,5} = 0.01$) are coincident early in the discharge. For the 8 MW/m^3 and 16 MW/m^3 heating cases, the spoiled symmetry configuration disrupts earlier. For the 2 MW/m^3 and 4 MW/m^3 heating cases, neither the helically symmetric nor the spoiled symmetry configurations disrupts.

relatively steady $\beta \approx 1.5\%$ as shown in Figure 16. The pressure profiles are also very similar between the helically symmetric and spoiled symmetry cases, with the temperature rising and peaking in the core, then relaxing to a more plateau-like profile. This cycle continues to repeat throughout the duration of the simulation and is shown in Figure 18 for the helically symmetric case. This cycle coincides with the oscillation between a state with an m=2, n=1 magnetic structure and one with partially-recovered flux surfaces in the core region.

Like the 4 MW/m^3 cases, no disruption is observed in the 2 MW/m^3 cases. In the helically symmetric case, no mode formation is observed, based on observation of the Poincaré plots.

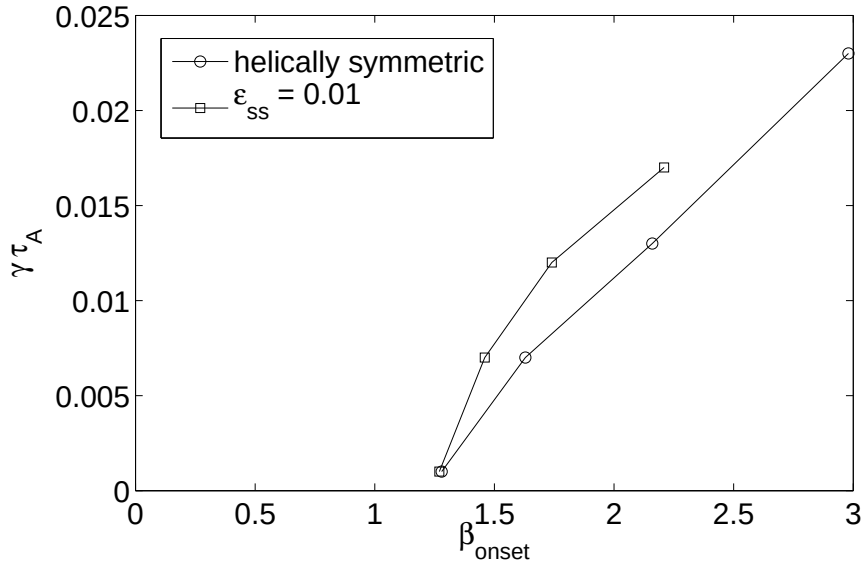

FIG. 17. Relationship between growth rate and onset beta for the m=2, n=2, $\epsilon_{22} = 0.87$ cases. The four data points for each series correspond to the four different heating rates. The largest heating rates result in the largest growth rates. The four lowest growth rate cases do not disrupt. Instead the instability nonlinearly saturates. For the two cases that have growth rate of 0.007, the equilibrium magnetic field reconfigures itself in response to the instability growth. It appears that the critical value of beta, for which no instability forms, is about 1.25%.

However, examination of the Fourier-decomposed parallel current shows mode formation, but the mode saturates at a low level. The final Poincaré plot looks identical to that at t = 0. The spoiled symmetry case does show some mode formation as evidenced by Poincaré plots, however these islands heal, with the final quiescent magnetic topology nearly identical to that of the vacuum. Even given these differences, in the end the spoiled symmetry case and helically symmetric case have identical final temperature profiles, and identical values of steady state beta.

All of these m=2, n=2, $\epsilon = 0.87$ cases display different behavior than the configuration with $\epsilon = 0.85$. First, although the values of β_{onset} are similar for each respective heating

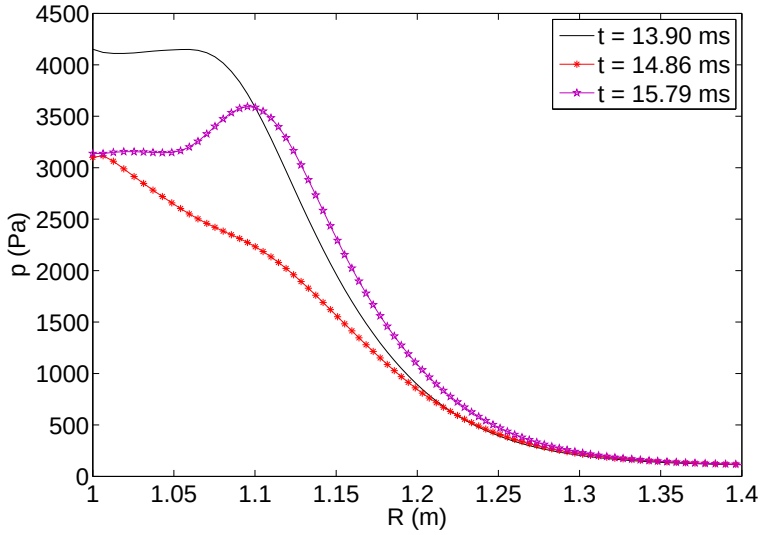

FIG. 18. (Color online) Pressure profiles of helically symmetric 4 MW/m^3 m=2, n=2, $\epsilon_{22} = 0.87$ case at selected times, $\zeta = 0$. The fluctuations coincide with oscillations in the magnetic topology between an m=2, n=1 non-resonant structure and recovered well-formed flux surfaces in the core region. Here, the magnetic axis is at R=1m.

rate, the growth rates of the n=1 instability in this present configuration are lower by 20 - 35%. Next, the 4 MW/m^3 cases do not disrupt for these $\epsilon = 0.87$ cases, in contrast with the $\epsilon = 0.85$ case. Finally, regarding onset beta, the addition of the symmetry-spoiling harmonics has a larger effect for higher heating rates in this $\epsilon = 0.87$ configuration compared with the $\epsilon = 0.85$ configuration. The symmetry-spoiling harmonics trigger mode formation at significantly lower levels of beta at higher heating rates, but this effect disappears for cases that are close to marginality.

B. The effect of changing anisotropic heat conduction.

Since a small degradation of the edge magnetic structure may be involved in limiting the drive the for instability growth, the degree of parallel transport is critical. In the current framework, the ratio of $\kappa_\parallel/\kappa_\perp$ can be thought of as a measure of how efficiently open field-lines carry energy out of the system. Changing the ratio of $\kappa_\parallel/\kappa_\perp$ changes the confinement properties for cases which do not consist completely of well-formed flux surfaces. Since decreasing $\kappa_\parallel/\kappa_\perp$ allows less heat to escape along open fieldlines at the plasma edge, decreasing $\kappa_\parallel/\kappa_\perp$ is akin to increasing the heating rate. Here, we adjust the ratio $\kappa_\parallel/\kappa_\perp$ by holding $\kappa_\perp$ fixed and changing $\kappa_\parallel$. Further, if the symmetry-spoiling harmonics are only measurably modifying physical processes in the edge region, e.g. contributing to flux surface destruction, their effect should be observed to be linked with the ratio of $\kappa_\parallel/\kappa_\perp$.

While changing the ratio of $\kappa_\parallel/\kappa_\perp$ changes the confinement properties for cases with broken flux surfaces, the addition of symmetry-spoiling harmonics does little to change the overall confinement properties as shown in Figure 19. Here, confinement time is determined by fitting an exponential function to the rise in pressure as the configuration is heated. That is, $3/2nkT = \tau_E Q(1 - \exp(-t/\tau_E))$, where Q is the heating rate, and τ_E is the confinement time. The rise in pressure computed here includes some flux surface destruction as beta increases. However, as $\kappa_\parallel/\kappa_\perp$ is decreased, the effects of the symmetry-spoiling harmonics become a little more pronounced as shown in Table I, in effect limiting the values that beta can achieve and thus limiting the growth rates of the instabilities. For example, see Figure 17, where at higher heating rates the symmetry-spoiling had a larger effect in terms of both β_{onset} and $\gamma\tau_A$.

Conversely, increasing $\kappa_\parallel/\kappa_\perp$ minimizes the effects of the strength of the symmetry-

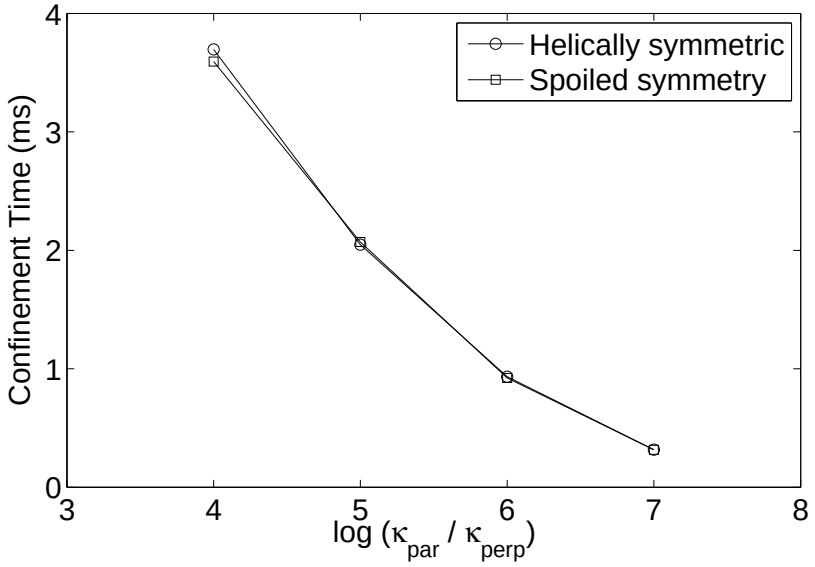

FIG. 19. The effect of anisotropic transport and symmetry-spoiling on confinement time.

TABLE I. The effect of parallel conductivity for the cases with dominant harmonic of m=2, n=2, $\epsilon_{22} = 0.87$, heating rate of 8 MW/m^3.

Symmetry	$\kappa_\parallel/\kappa_\perp$	$\beta_{\max}$ (%)	β_{onset} (%)	$\gamma\tau_A$
Helically Symmetric	10^4	4.35	3.58	0.012
	10^5	3.40	2.97	0.014
	10^6	2.28	2.16	0.013
	10^7	1.32	1.31	0.004
$\epsilon_{5,1} = \epsilon_{6,1} = \epsilon_{6,5} = 0.01$	10^4	3.15	2.43	0.010
	10^5	3.15	2.46	0.013
	10^6	2.12	1.74	0.012
	10^7	1.33	1.30	0.006

spoiling harmonics as shown in Table I. Again, this is akin to the minimal effect of the

symmetry-spoiling harmonics at lower heating rates as shown in Figure 17.

V. DISCUSSION

Finite beta simulations of a straight stellarator have been conducted to examine the effect of 3-D magnetic fields on the equilibrium and stability of helically symmetric fields. The notions of equilibrium and stability become intertwined in configurations such as this, as the equilibrium magnetic field changes in response to increasing beta. The changing equilibrium magnetic field changes the associated stability properties. Small changes in the vacuum magnetic field and changes in the temperature (and the resulting conductivity) can greatly affect the robustness of the configuration to developing instabilities.

In the simulation results reported here, heat is added to the plasma and beta increases until some MHD stability boundary is traversed, at which time an instability appears. In many of the cases, this instability is a non-resonant core mode, rather than a mode localized about some rational surface. This core mode acts to quickly pump heat out of the plasma. At this point either disruption ensues, or the plasma displays recovery in a manner similar to a sawtooth in a tokamak. This recovery can be complete in that well-formed flux surfaces reappear everywhere. Or, in some cases, the recovery is only partial, where some good flux surfaces are recovered, but stochastic regions or magnetic islands remain. This time-dependent transport-related push and pull between the equilibrium magnetic field structure and the persistent instability is a key feature of 3D magnetic configurations, and is the primary aim of these investigations.

The addition of small symmetry-spoiling, or 3-D, harmonics to the equilibrium magnetic field has been shown to affect the evolution of finite-beta discharges. A general trend has been shown for cases where the core vacuum rotational transform is near 1/2. The symmetry-

spoiling effects tend to reduce the peak beta that is achieved, the value of beta at which mode growth is triggered, and also to reduce the growth rate, although this effect is more pronounced for higher growth rates.

We surmise that there are two possible mechanisms by which the addition of symmetry-spoiling harmonics affect discharge evolution. One possibility is that these symmetry-spoiling harmonics act as a safety valve in the edge region. Since the symmetry-spoiling harmonics are small, confinement properties are largely still retained, but not to quite the same degree that would be expected from well-formed flux surfaces. That is, confinement is slightly degraded at the edge, thus limiting the pressure gradient that can develop within the plasma. This pressure-flattening modification to the equilibrium is similar to that discussed by Ichiguchi.[3]. The pressure profile (and thus the equilibrium) self-consistently changes or "self-organizes" in response to heating. These changes leave a resulting equilibrium which is more robust to low-n interchange modes.

Another possibility is that these symmetry-spoiling harmonics add to the magnetic energy for specific n-harmonics, and as a result alter some critical MHD threshold for instability formation and growth. The resulting core mode forms sooner, but grows a little more slowly since beta is somewhat smaller. This leads to energy being transported out of the core region as the mode grows, limiting beta and limiting the drive for further instability growth. This mechanism is further supported by the results of Section IV B, where the effect of the symmetry-spoiling harmonics is not enhanced at higher levels of $\kappa_{\|}/\kappa_{\perp}$ for cases where non-resonant modes appear. If the stochastic edge region acted as a safety valve and limited the value of beta in the plasma, a larger value of $\kappa_{\|}/\kappa_{\perp}$ would presumably enhance the contribution of the symmetry-spoiling harmonics. Instead, the mechanism proposed here is that enough energy must build to trigger the formation of an MHD mode. The presence of

symmetry-spoiling harmonics lowers this threshold, triggering core mode formation earlier than without the symmetry-spoiling harmonics. This mode grows and transports energy out of the plasma before enough energy can build to cause higher growth rates from which the equilibrium cannot recover.

Both of the mechanisms are likely at work. The first mechanism above, proposed by Ichiguchi, appears to be dominant for instabilities which are resonant. Whereas, the second mechanism proposed here appears to be dominant for instabilities which are non resonant.

These mechanisms can be used to explain why W7-AS achieved such large values of beta when instability was predicted to cause disruption[2,29,30]. In these cases, the onset and growth of a destructive m=2 pressure-driven mode was predicted to destroy W7-AS plasmas at relatively low values of beta. However, a disruption caused by these instabilities was avoided as the equilibrium changed over time. Symmetry spoiling effects which slightly degrade the magnetic field could contribute to stabilization of this mode.

The computations presented here lay the framework for more comprehensive study of how 3-D configurations respond to emerging instabilities. Further studies should look at more experimentally relevant heating profiles and perpendicular fluxes (which may be anomalous), as well as the inclusion of temperature-dependent resistivity and temperature dependent conductivities. Toroidal geometry effects can be investigated, as in our extended MHD calculations of current-driven flux surface evolution.[22] Additionally, opportunities exist to quantify predictions of the effect of plasma flow on the magnetic topology of 3-D configurations.[20,21] And, future studies which explore the relationship between the Mercier stability parameter, D_I, and how the equilibrium responds may provide additional insights.

ACKNOWLEDGMENTS

This work is supported by the U.S. Department of Energy, Grant No. DE-FG02-99ER54546, and this research used resources of the National Energy Research Scientific Computing Center, which is supported by the Office of Science of the U.S. Department of Energy under Contract No. DE-AC02-05CH11231.

REFERENCES

[1]H. Yamada, Nuclear Fusion **51**, 94021 (2011).

[2]A. Weller, S. Sakakibara, K. Y. Watanabe, K. Toi, J. Geiger, M. C. Zarnstorff, S. R. Hudson, A. Reiman, A. Werner, C. Nuhrenberg, S. Ohdachi, Y. Suzuki, and H. Yamada, Fusion Science and Technology **50**, 158 (2006).

[3]K. Ichiguchi and B. A. Carreras, Nuclear Fusion **51**, 53021 (2011).

[4]A. Reiman, M. C. Zarnstorff, D. Monticello, A. Weller, and J. Geiger, Nuclear Fusion **47**, 572 (2007).

[5]F. Troyon and R. Gruber, Physics Letters A Phys. Lett. A (Netherlands), **110A**, 29 (1985).

[6]H. Grad, Physics of Fluids **10**, 137 (1967).

[7]A. Schlüter and U. Schwenn, Computer Physics Communications **24**, 263 (1981).

[8]S. P. Hirshman, W. I. van RIJ, and P. Merkel, Computer Physics Communications **43**, 143 (1986).

[9]T. C. Hender, B. A. Carreras, L. Garcia, J. A. Rome, and V. E. Lynch, Journal of Computational Physics **60**, 76 (1985).

[10]H. S. Greenside, A. H. Reiman, and A. Salas, Journal of Computational Physics **81**, 102 (1989).

[11]P. R. Garabedian, Phys.Plasmas **9**, 137 (2002).

[12]O. Fischer and W. A. Cooper, Plasma Physics and Controlled Fusion **40**, 1269 (1998).

[13]R. Chodura and A. Schlüter, Journal of Computational Physics **41**, 68 (1981).

[14]A. Reiman and H. Greenside, Computer Physics Communications **43**, 157 (1986).

[15]K. Harafuji, T. Hayashi, and T. Sato, Journal of Computational Physics **81**, 169 (1989).

[16]S. P. Hirshman, R. Sanchez, and C. R. Cook, Physics of Plasmas **18**, 62504 (2011).

[17]S. R. Hudson, R. L. Dewar, M. J. Hole, and M. McGann, Plasma Physics and Controlled Fusion **54**, 14005 (2012).

[18]S. R. Hudson and N. Nakajima, Physics of Plasmas **17**, 52511 (2010).

[19]Y. Narushima, F. Castejón, S. Sakakibara, K. Y. Watanabe, S. Ohdachi, Y. Suzuki, T. Estrada, F. Medina, D. López-Bruna, M. Yokoyama, M. Yoshinuma, K. Ida, S. Nishimura, L. H. D. E. Group, and T.-I. E. Group, Nuclear Fusion **51**, 83030 (2011).

[20]C. C. Hegna, Nuclear Fusion **51**, 113017 (2011).

[21]C. C. Hegna, Physics of Plasmas **19**, 56101 (2012).

[22]M. G. Schlutt, C. C. Hegna, C. R. Sovinec, S. F. Knowlton, and J. D. Hebert, Nuclear Fusion **52**, 103023 (2012).

[23]C. R. Sovinec, A. H. Glasser, T. A. Gianakon, D. C. Barnes, R. A. Nebel, S. E. Kruger, D. D. Schnack, S. J. Plimpton, A. Tarditi, and M. S. Chu, Journal of Computational Physics **195**, 355 (2004).

[24]R. Fitzpatrick, Phys.Plasmas **2**, 825 (1995).

[25]N. N. Gorelenkov, R. V. Budny, Z. Chang, M. V. Gorelenkova, and L. E. Zakharov, Phys.Plasmas **3**, 3379 (1996).

[26]M. G. Schlutt and C. C. Hegna, Physics of Plasmas **19**, 82514 (2012).

[27]V. D. Shafranov, Phys.Fluids **26**, 357 (1983).

[28]T. Tatsuno, M. Wakatani, and K. Ichiguchi, Nuclear Fusion **39**, 1391 (1999).

[29]K. Ichiguchi., N.Nakajima, M.Wakatani, B.A.Carreras, and V. Lynch, Nuclear Fusion **43**, 1101 (2003).

[30]K. Y. Watanabe, A. Weller, S. Sakakibara, Y. Narushima, S. Ohdachi, K. Narihara, K. Tanaka, K. Ida, K. Toi, H. Yamada, Y. Suzuki, and O. Kaneko, in *Fourteenth International Stellarator Workshop*, Vol. 46 (ANS, Nat. Inst. for Fusion Sci., Toki, Japan, 2004) pp. 24–33.